

Accepted Manuscript

Microstructure evolution of T91 irradiated in the BOR60 fast reactor

Z. Jiao, S. Taller, K. Field, G. Yeli, M.P. Moody, G.S. Was

PII: S0022-3115(18)30180-6

DOI: [10.1016/j.jnucmat.2018.03.024](https://doi.org/10.1016/j.jnucmat.2018.03.024)

Reference: NUMA 50845

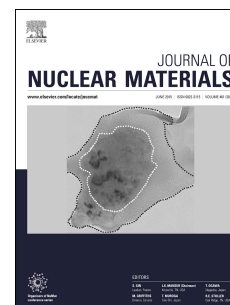
To appear in: *Journal of Nuclear Materials*

Received Date: 5 February 2018

Accepted Date: 13 March 2018

Please cite this article as: Z. Jiao, S. Taller, K. Field, G. Yeli, M.P. Moody, G.S. Was, Microstructure evolution of T91 irradiated in the BOR60 fast reactor, *Journal of Nuclear Materials* (2018), doi: 10.1016/j.jnucmat.2018.03.024.

This is a PDF file of an unedited manuscript that has been accepted for publication. As a service to our customers we are providing this early version of the manuscript. The manuscript will undergo copyediting, typesetting, and review of the resulting proof before it is published in its final form. Please note that during the production process errors may be discovered which could affect the content, and all legal disclaimers that apply to the journal pertain.



Microstructure Evolution of T91 Irradiated in the BOR60 Fast Reactor

Z. Jiao^{a,*}, S. Taller^a, K. Field^b, G. Yeli^c, M. P. Moody^c, G. S. Was^a

^aDepartment of Nuclear Engineering and Radiological Sciences, University of Michigan, Ann Arbor, MI, US

^bMaterials Science & Technology Division, Oak Ridge National Laboratory, TN, US

^cDepartment of Materials, University of Oxford, Parks Road, OX1 3PH, UK

Abstract

Microstructures of T91 neutron irradiated in the BOR60 reactor at five temperatures between 376°C and 524°C to doses between 15.4 and 35.1 dpa were characterized using transmission electron microscopy (TEM), scanning transmission electron microscopy (STEM), and atom probe tomography (APT). Type $a\langle 100 \rangle$ dislocation loops were observed at 376-415°C and network dislocations dominated at 460°C and 524°C. Cavities appeared in a bimodal distribution with a high density of small bubbles less than 2 nm at irradiation temperatures between 376°C and 415°C. Small bubbles were also observed at 460°C and 524°C but cavities greater than 2 nm were absent. Enrichment of Cr, Ni, and Si at the grain boundary was observed at all irradiation temperatures. Radiation-induced segregation (RIS) of Cr, Ni and Si appeared to saturate at 17.1 dpa and 376°C. The temperature dependence of RIS of Cr, Ni and Si at the grain boundary, which showed a peak Cr enrichment temperature of 460°C and a lower peak Ni and Si enrichment temperature of ~400°C, was consistent with observations of RIS of Cr in proton irradiated T91, suggesting that the same RIS mechanism may also apply to BOR60 irradiated T91. G-phase and Cu-rich precipitates were observed at 376-415°C but were absent at 460°C and 524°C. The absence of G-phase at 524°C could be related to the minimal segregation of Ni and Si in that condition.

Keywords: Microstructure; Radiation-induced segregation; Swelling; Radiation-induced precipitates

*Corresponding Author:

Phone: +1-734-615-7761; Fax: +1-734-763-4540 Email: zjiao@umich.edu

[†]This manuscript has been authored in-part by UT-Battelle, LLC under Contract No. DE-AC05-00OR22725 with the U.S. Department of Energy. The United States Government retains and the publisher, by accepting the article for publication, acknowledges that the United States Government retains a non-exclusive, paid-up, irrevocable, world-wide license to publish or reproduce the published form of this manuscript, or allow others to do so, for United States Government purposes. The Department of Energy will provide public access to these results of federally sponsored research in accordance with the DOE Public Access Plan (<http://energy.gov/downloads/doe-public-access-plan>).

1. Introduction

Fission reactor concepts such as the sodium fast reactor (SFR), molten salt reactor (MSR), and the traveling wave reactor (TWR), require that structural materials survive at irradiation damage levels in excess of 200 dpa (displacement per atom) at temperatures exceeding 400°C. Microstructure evolution and microstructure-related degradation modes must be understood for reliable materials performance at this high dpa level. High damage rate ion irradiation is the only viable means to conduct accelerated testing to assess irradiated microstructures at high dpa levels, and has demonstrated great potential in reproducing the microstructure of alloy HT9 irradiated in reactor [1]. An integrated research project (IRP) involving international collaboration among multiple universities, national laboratories and industry partners, was initiated in 2013 [2]. The goal of the IRP is to demonstrate the capability of ion irradiation to predict the evolution of microstructure and properties of a range of structural materials in reactor and at high doses. One of the major research activities of the program was to benchmark ion irradiations against neutron irradiations using the same heat of ferritic-martensitic (F-M) steel, T91. Hence, reactor irradiation and post-irradiation microstructure characterization are critical for the success of the program. Reactor irradiations are conducted in the BOR60 fast reactor in Russia [3] that produces 15-20 dpa/yr and ~100 dpa for the full irradiation period of 5 yrs.

T91 is one of the candidate materials for high dose structural components application because F-M alloys exhibit excellent swelling resistances compared to austenitic steels [4]. The major degradation modes in alloy T91 are likely to be dimensional instability caused by void swelling and/or embrittlement due to phase stability at high dpa levels. The reactor-irradiated microstructure of T91 has been investigated in a few studies [5-12], most of which were focused on void swelling and radiation-induced precipitation. Dislocation loops were characterized in some cases [6,8,11,12] but radiation-induced segregation (RIS) at grain boundaries was not investigated in any of these studies. The biggest deficiency in the literature data is the lack of consistency between data sets, as they involve multiple reactors and/or multiple heats of T91. Consequently, microstructure evolution with dose or temperature cannot be reliably determined from the existing literature data. Irradiations in the same reactor of BOR60 using the same heat of T91 would eliminate the variables thus make it possible for a systematic study of microstructure evolution with irradiation dose and temperature.

The objective of this study is to develop a better understanding of the overall irradiated microstructure, including dislocation loops, cavities, and precipitates as well as RIS, evolution with irradiation dose and temperature for the same heat of T91 irradiated in BOR60, and also to provide a substantive set of irradiated microstructure data for a comprehensive comparison of ion and neutron irradiation effects.

2. Experiments

2.1 Sample preparation and BOR60 irradiation

Alloy T91, heat 30176, used in this study was received from Pacific Northwest National Laboratory (PNNL). The chemical compositions provided by PNNL and an independent analysis by Luvak Inc. are given in Table 1. The major discrepancies are the Si and Cu contents. Luvak analysis shows much higher Si content (0.25%) than that provided by PNNL (0.11%). The Luvak analysis also shows 0.062% of Cu and it was not reported in the PNNL analysis. The as-received T91 samples were encapsulated in a quartz tube that was evacuated and then backfilled with 0.25 atmosphere of helium. The samples were then normalized at 1038°C for 30 minutes and air cooled. Tempering was performed at 760°C for 30 minutes and then air cooled. The countdown for the heat treating began when the temperature of a thermocouple touching the quartz tube came within 5°C of the target temperature. Slices of thickness of 0.4 mm were cut from the heat-treated T91 samples using wire electrical discharge machining (EDM) and were thinned down to 0.25 mm by double sided diamond lapping to a 0.25 μm finish. 3-mm diameter disks were then punched out from the thinned slices using a Gatan TEM disc punch system. Each of the disks was then laser engraved for identification before they were loaded into capsules for BOR60 irradiation.

The TEM capsules were inserted into the BOR60 reactor at different reactor core positions to achieve various irradiation temperatures. The targeted irradiation temperatures were 370, 400, 450 and 525°C and the targeted doses were 20 and 40 dpa. All the TEM capsules went through multiple irradiation cycles. Actual sample temperatures were calculated based on the coolant temperature reported at each irradiation cycle and the calculated temperature rise through the capsule to the TEM samples. Irradiation doses were calculated based on the integral of the displacement cross section and the BOR60 neutron energy spectrum. There were slight cycle-to-

cycle variations in sample temperature ($<10^{\circ}\text{C}$) and the durations at each cycle also varied from 9 to 83 days. The weighted average irradiation temperatures and the accumulated irradiation doses at retrieval were $376^{\circ}\text{C}:17.1\text{dpa}$ (irradiation temperature : final irradiation dose); $378^{\circ}\text{C}:35.1\text{dpa}$, $415^{\circ}\text{C}:18.6\text{dpa}$, $460^{\circ}\text{C}:14.6\text{dpa}$ and $524^{\circ}\text{C}:15.4\text{dpa}$ with dose rates ranging from $6\text{--}9\times 10^{-7}\text{ dpa/s}$.

2.2 Post-irradiation examination

BOR60 irradiated T91 samples were received and characterized at the Low Activation Materials Development and Analysis (LAMDA) laboratory at the Oak Ridge National Laboratory (ORNL) [13]. Transmission electron microscopy (TEM) foils for microstructure and microchemistry characterization were prepared using an FEI Versa DualBeam focused ion beam (FIB) system. FIB lift-out, instead of traditional electropolishing/jet-thinning method, was used to achieve minimal sample volume to minimize magnetism and sample radioactivity. Two critical steps were adapted for preparation of high quality TEM foils which minimized FIB damage using the FIB lift-out method. The first was to create a thick window frame to prevent foil bending and twisting during sample thinning below a thickness of $\sim 300\text{ nm}$. The second was to use a low energy ion beam (5 keV and 2 keV) when the foil was still relatively thick (around 150 nm) to thin the foil to a final thickness around 100 nm , which effectively eliminated TEM-visible FIB damages induced at high beam energy.

Dislocation loops and cavities were characterized using the JEOL 2100F TEM/STEM (scanning transmission electron microscopy) at the LAMDA laboratory. The STEM-BF (bright field) technique was used for dislocation imaging as it resulted in reduced strain contrast compared to the traditional TEM two-beam BF technique [14,15]. As the majority of dislocation loops in irradiated F-M steels are of the type $a<100>$, they were characterized using either the $<001>$ or $<011>$ zone axis, under which a fraction ($2/3$ under $<001>$ zone axis and $1/3$ under $<011>$ zone axis) of $a<100>$ loops appear edge-on in the image [16]. Cavities were characterized using high-angle annular dark-field scanning transmission electron microscopy (HAADF-STEM). Additional characterization was performed on the JEOL 2010F at the Michigan Center for Materials Characterization facility at the University of Michigan to identify cavities smaller than 2 nm in diameter using overfocused and underfocused bright field TEM imaging. Hand-counting techniques were used with the ImageJ software to measure the cavity diameter and estimate the

density. The swelling was calculated from the HAADF-STEM images using the following equation:

$$\frac{\Delta V}{V} = \frac{\frac{\pi}{6} \sum_{i=1}^N d_i^3}{A\delta - \frac{\pi}{6} \sum_{i=1}^N d_i^3} * 100 \quad \text{Eq. 1}$$

Where A is the area of the images, δ is the foil thickness, d_i is the cavity diameter, and N is the number of cavities. The foil thickness was measured in the STEM mode using the electron energy loss spectroscopy (EELS) zero loss method.

Radiation-induced segregation at grain boundaries was characterized using the FEI Talos F200X scanning/transmission electron microscope (S/TEM) instrument equipped with high counting rate energy dispersive x-ray spectroscopy (EDS). Prior to RIS measurements, random lath boundaries were selected and tilted to edge-on position by minimizing the projected width of the grain boundary. EDS-based spectrum images were taken from the lath boundaries using a region-of-interest size of 1024×1024 pixels with a resolution of ~0.23 nm/pixels with a probe full width half max of ~1.5 nm and a beam current around 3nA. Each scan had a duration of one hour with more than 35,000 counts/sec with dead times from 1-6%. The qualitative x-rays counts were converted to quantified weight percentages using the Bruker Esprit© 1.9 software package, which used the Cliff-Lorimer [17] calculations for each pixel. Line scans were produced from the region-of-interest scan by binning multiple quantitative weight percentages in a 50-pixel line parallel to the boundary and 5 pixels perpendicular to the boundary achieve about 1.1 nm spacing between points in the line scan. RIS at two grain boundaries was measured for all conditions except for the 35.1 dpa: 378°C condition, in which only one grain boundary was characterized. No significant variation in grain boundary composition was observed between the two grain boundaries at the same irradiation conditions. EDS maps were also obtained from the matrix for precipitate characterization (including both pre-existing carbides/nitrides and radiation-induced precipitates). The sizes of dislocation loops, cavities and precipitates were measured from TEM/STEM/EDS-based images using hand-counting techniques and the ImageJ software.

The nature of radiation-induced precipitates was characterized using atom probe tomography (APT). Specimens for analysis were prepared using a dual beam microscope FEI Helios NanoLab 600i at Culham Center for Fusion Energy (CCFE), the UK's national fusion research laboratory. All specimens were taken between 400 nm - 800 nm beneath the surface.

APT analysis was carried out on a CAMECA LEAP 5000XR at University of Oxford. Voltage pulsing mode with 20 % pulse fraction was used. Reconstruction of atom maps and composition analysis of the precipitates from the raw data was performed using the commercial software, IVAS from CAMECA.

3. Results

The unirradiated microstructure of T91 in the as-tempered condition consisted of prior austenite grain boundaries, packets, laths, coarse chromium carbides, fine V,Cr-nitrides, and network dislocations. Chromium carbides were mainly $M_{23}C_6$ type and were mostly on the prior austenite grain boundaries (PAGBs) or lath boundaries. Fine V,Cr-nitrides were observed in the matrix and sometimes were found adjacent to the Cr-carbides. The average size of $M_{23}C_6$ was estimated to be ~ 100 nm while the average size for (V,Cr)N was approximately 40 nm. Both Cr-carbides and V,Cr-nitrides had an estimated number density between 10^{18} m^{-3} and 10^{19} m^{-3} based on the EDS-based spectrum images and foil thickness measurements. The dislocation density varied from area-to-area and was estimated to be $\sim 10^{15} \text{ m}^{-2}$.

3.1 Dislocation loops

STEM-BF images of dislocation loops under different BOR60 irradiation conditions are shown in Fig. 1a-c and a summary of the average dislocation loop diameter and number density is given in Table 2. Images of dislocation loops for BOR60 irradiated T91 at $376^\circ\text{C}:17.1\text{dpa}$ and $378^\circ\text{C}:35.1\text{dpa}$ are shown in Fig. 1a and Fig. 1b, respectively. Both images were taken near the $\langle 100 \rangle$ zone axis and thus loops with a Burgers vector of $a\langle 100 \rangle$ on (010) and (001) planes appeared as nearly edge-on in the images as indicated by arrows. Both irradiation conditions show the dominance of $a\langle 100 \rangle$ loops compared to loops with Burgers vector $a/2\langle 111 \rangle$. The average dislocation loop diameters are 21.8 nm and 22.9 nm and the number densities are $2.9 \times 10^{21} \text{ m}^{-3}$ and $1.9 \times 10^{21} \text{ m}^{-3}$ for 17.1 dpa and 35.1 dpa, respectively. The loop size distributions for these two irradiation doses are shown in Fig. 1f. The slight increase in average loop diameter and decrease in number density at 35.1 dpa were mainly due to the absence of smaller loops (< 10 nm) in this condition, although the number density appeared to drop in nearly all the loop size bins. Besides $a\langle 100 \rangle$ loops, a possible $1/2a\langle 111 \rangle$ loop that did not show up as

edge-on in the image and did not align with other $a\langle 100 \rangle$ loops is circled in Fig. 1a. The density of $1/2a\langle 111 \rangle$ loops was estimated to be less than 10% of the $a\langle 100 \rangle$ loop density.

Fig. 1c shows dislocation loops in T91 irradiated at 415°C:18.6 dpa. The image was taken near the $\langle 110 \rangle$ zone axis and thus only $a\langle 100 \rangle$ loops on (001) planes appeared edge-on. The average dislocation loop diameter and number density were 25.8 nm and $2.0 \times 10^{21} \text{ m}^{-3}$, respectively. The average loop diameter increased and the number density decreased compared to the lower temperature irradiation (376°C:17.1 dpa), as indicated by a shift in the loop size distribution shifted to larger loop size (Fig. 1f). Fig. 1d and Fig. 1e show dislocation images in T91 irradiated at 460°C:14.6 dpa, and at 524°C:15.4 dpa, respectively. No dislocation loops were identifiable. Network dislocations appeared to be the dominant dislocation microstructure. There was significant area-to-area variation in network dislocation density for all irradiation conditions, typically in the range of $\sim 5 \times 10^{14} \sim 5 \times 10^{15} \text{ m}^{-2}$. Irradiation at the examined irradiation conditions did not seem to significantly alter the existing network dislocation density from the as-received condition.

3.2 Cavities

STEM-HAADF images of cavities in T91 irradiated in BOR60 under different irradiation conditions are shown in Fig. 2. Some cavities (dark contrast in the HAADF imaging conditions) are indicated by arrows in Fig. 2a-2c. The STEM-HAADF technique can effectively reveal cavities greater than 2 nm but smaller cavities can be easily missed due to the weak contrast. Underfocus TEM BF technique is capable of imaging cavities less than 2 nm, although the exact size of cavities cannot be accurately determined without proper simulation tools due to the large amount of under focus, which may exceed 1 μm . The inset in Fig. 2a shows a high density of small cavities as revealed by underfocus TEM BF technique for the 376°C:17.1dpa irradiation condition. The number density for cavities greater than 2 nm was $7.3 \times 10^{20} \text{ m}^{-3}$ while the number density of smaller cavities (presumably helium bubbles – although not confirmed in this study) was $1.2 \times 10^{23} \text{ m}^{-3}$ (Table 2), or more than two orders of magnitude higher compared to the larger cavity distribution. For the convenience of discussion, cavities greater than 2 nm are hereafter referred to as “voids” while cavities smaller than 2 nm are referred to as “bubbles”. Voids were observed at the 376°C:17.1dpa, 378°C:35.1dpa and 415°C:18.6dpa conditions. The average void size was 6.9 nm at 376°C:17.1 dpa and was virtually unchanged when the irradiation dose was

increased to 35.1 dpa (6.5 nm). However, the void density nearly doubled ($7.3 \times 10^{20} \text{ m}^{-3}$ at 17.1 dpa vs. $1.5 \times 10^{21} \text{ m}^{-3}$ at 35.1 dpa) while the bubble density decreased from $1.2 \times 10^{23} \text{ m}^{-3}$ to $2.2 \times 10^{22} \text{ m}^{-3}$ as irradiation dose increased (Table 2). Void size and number density as well as the bubble density were smaller at the higher irradiation temperature of 415°C. The presence of a high density of small bubbles resulted in a bimodal cavity distribution, Fig. 2f. No voids were observed at the 460°C:14.6 dpa condition but small bubbles are observed with a number density of $3.2 \times 10^{21} \text{ m}^{-3}$. Small bubbles with an estimated number density of $3.3 \times 10^{21} \text{ m}^{-3}$ were also observed in the 524°C:15.4 dpa condition. Void swelling was 0.016% at 376°C:17.1 dpa and it increased to 0.033% at 378°C:35.1 dpa (Table 2). Swelling was much lower (0.006%) at 415°C:18.6 dpa.

Voids exhibited large area-to-area (lath-to-lath or different areas within the same lath) variations particularly when the number density was low (Fig. 2c). In fact, not all the laths showed the presence of voids in the STEM-HAADF images at a magnification of 150kx. The fraction of laths that showed nucleation of voids was ~80% for both 376°C:17.1dpa and 415°C:18.6 dpa irradiation conditions. As the irradiation dose increased to 35.1 dpa at 378°C, nearly all the laths exhibited voids.

3.3. Pre-existing carbides/nitrides and radiation-induced precipitates

Both pre-existing Cr-carbides and V,Cr-nitrides remained after BOR60 irradiation as evidenced by the EDS elemental maps in Fig. 3a for the 376°C:17.1dpa irradiation and Fig. 3b for the 460°C:14.6dpa irradiation. The number density of Cr,V-nitrides is slightly higher than that of Cr-carbides but both are in the order of 10^{18} - 10^{19} m^{-3} , which is the same order of magnitude as in the unirradiated state. There are large variations in both precipitate size and density at different irradiation conditions or different EDS-based spectrum images from different areas of the same sample. Because of the large variations mainly due to poor statistics, the irradiation effect(s) on pre-existing precipitates is inconclusive.

The major radiation-induced precipitates are the Ni/Si-rich precipitates which can be observed from the Ni and Si maps in Fig. 3a. Evolution of the Ni/Si-rich precipitates at different irradiation conditions is shown in Fig. 4. The distribution of Ni/Si-rich precipitates is shown in Fig. 4f. The average precipitate size increased slightly from 5.8 nm at 376°C:17.1dpa to 7.0 nm at 378°C:35.1dpa while the number density slightly decreased from $3.6 \times 10^{21} \text{ m}^{-3}$ to $2.4 \times 10^{21} \text{ m}^{-3}$.

Irradiation at 415°C:18.6 dpa resulted in slightly larger precipitates (6.7 nm) with lower density ($3.0 \times 10^{21} \text{ m}^{-3}$) compared to the 376°C:17.1dpa irradiation. Cu-rich precipitates were also observed in T91 irradiated at lower temperatures (376- 415°C). Cu clustering was not observed at either 460°C or 524°C.

The nature of radiation-induced precipitates was further examined using APT. Fig. 5 shows the presence of Ni/Si/Mn-rich and Cu-rich precipitates in T91 irradiated at 415°C:18.6 dpa. Ni/Si/Mn-rich clusters are highlighted using iso-concentration surfaces of Mn + Ni + Si at 5 at% in Fig. 6a and 6c for two different APT tips. Composition proximity histograms of Cluster 1 in Fig. 6a and Cluster 2 in Fig. 6c are plotted in Fig. 6b and Fig. 6d, respectively. The core region of Cluster 2 contains around 40 at% Ni, 20 at% Si and 10 at% Mn (Fig. 6d), which is close to the composition G-phase ($\text{Mn}_6\text{Ni}_{16}\text{Si}_7$ with ~21 at% Mn, 55 at% Ni and 24 at% Si). Cluster 1 in Fig. 6b shows much lower Ni/Si/Mn concentration than that of G-phase. Therefore, if clusters of the type highlighted by APT in Fig. 6c correlate to the Ni/Si-rich clusters as revealed by EDS in Fig. 4, these are most likely to be a distribution of G-phase precursors.

3.4 Radiation-induced segregation at grain boundaries

Examples of EDS elemental count maps containing an edge-on lath boundary are shown in Fig. 7a and Fig. 7b for the 376°C:17.1dpa and 524°C:15.4dpa irradiation conditions, respectively. Depletion of Fe and enrichment of Cr at the grain boundary was apparent for both irradiation conditions. Enrichment of Ni and Si at the grain boundary was evident for the 376°C:17.1dpa irradiation but appeared to be minimal for the 524°C:15.4 dpa irradiation.

Composition profiles across the grain boundary for Fe, Cr, Ni and Si for all the irradiation conditions are shown in Fig. 8. Concentrations of Cr, Ni and Si at the grain boundary as well as the magnitude of depletion/enrichment are given in Table 2. Iron depleted at all the irradiation conditions with the maximum depletion occurring at 460°C. Enrichment of Cr was observed for all profiles with minimal enrichment of <3 wt% at 376-378°C and maximal enrichment of ~6 wt% at 460°C. Both Ni and Si enriched at the grain boundary but the enrichment was minimal at 524°C (~0.2 wt%). Enrichment of Cr, Ni and Si at the grain boundary as a function of temperature is shown in Fig. 9. Enrichment of Cr peaked around 460°C while Ni and Si appeared to peak at lower temperature. An increase in the irradiation dose

from 17.1 dpa to 35.1 dpa did not appear to affect the magnitude of enrichment for all three elements at 376-378°C (open and closed circle symbols in Fig. 9).

4. Discussion

4.1 Dislocation loop evolution

Dislocation loops in irradiated ferritic-martensitic (F-M) steels are typically interstitial type [18,19] with Burgers vector of either $1/2a\langle 111 \rangle$ or $a\langle 100 \rangle$. The fraction of $a\langle 100 \rangle$ loops increases with irradiation temperature [20,21] and they become dominant at 500°C in heavy ion irradiated Fe and Fe-Cr alloys [22]. The fraction of $a\langle 100 \rangle$ loops may also be affected by Cr content with predominance of $a\langle 100 \rangle$ observed in lower Cr alloys [6]. In BOR60 irradiated T91 in the temperature range 376-415°C, the dominant dislocation loops were type $a\langle 100 \rangle$. This is consistent with the observations by Kato et al. [23] who observed only $a\langle 100 \rangle$ dislocation loops in Fe-Cr binary ferritic alloys irradiated to 140 dpa at 425°C in the Materials Open Test Assembly in the Fast Flux Test Facility (FFTF). Sencer et al. [24] also confirmed the prevalence of $a\langle 100 \rangle$ loops in HT9 irradiated to 150 dpa at 443°C. The observations of the nature of loops in BOR60 appeared to be consistent with those in FFTF irradiated in a similar temperature range.

Dislocation loops typically saturate after a few dpa in stainless steels [25]. In-situ Intermediate Voltage Electron Microscope (IVEM) irradiation [26, 27] showed that dislocation loop density increased with dose initially and then saturated at ~6 dpa in F-M steel NF616. Proton irradiation in the temperature range 400-500°C [28] exhibited a saturation in dislocation loop density after a few dpa. Therefore, it is not surprising that a significant change in dislocation loop size and density was not observed when irradiation dose increased from 17.1 dpa to 35.1 dpa at 376-378°C in BOR60, Figure 8a. In fact, Getto et al. [29] showed that the dislocation loop density was nearly constant to very high dpa levels (188-650 dpa) in self-ion irradiated HT9.

The effect of irradiation temperature on dislocation loops in metals and alloys is well known [30]. The average loop size typically increases while the loop density decreases with irradiation temperature. The increase in dislocation loop size is evident in the size distribution plot of Figure 1f and in the average loop diameter in Fig. 11a. Network dislocations dominated at 460°C and 524°C in BOR60-irradiated T91. Henry and Maloy [18] noted that loops were observed up to irradiation temperatures in the range 400–450°C for fast reactors, while at higher

temperatures only network dislocations were present. The absence of dislocation loops at 460°C and 524°C in BOR60 irradiated T91 is consistent with their observations.

4.2 Cavity evolution

The average void size did not change but the number density nearly doubled when the irradiation dose increased from 17.1 dpa to 35.1 dpa at 376-378°C (Fig. 10b), indicating that voids were probably still in the nucleation stage at 17.1 dpa. Bubble density appeared to peak at 17.1 dpa as the density at 35.1 dpa dropped to ~1/5 of that at 17.1 dpa. Nucleation of voids may be due to the growth of some of the existing bubbles at lower dose. The average swelling rate up through 35.1 dpa was ~0.001%/dpa for BOR60 irradiated T91. The same heat of T91 (30176) irradiated in FFTF exhibited void swelling of 1.2-1.6% at 413°C to 184 dpa [9] and 1.9-2.6% at 400°C to 208 dpa [7], resulting in an average swelling rate of ~0.01%/dpa, about one order of magnitude higher than BOR60 irradiation at 17-35 dpa. This indicates that T91 samples irradiated in BOR60 were still in the swelling incubation period and probably far from the steady-state swelling regime, which is expected at these relatively lower doses. The wider size distribution at 35.1 dpa vs. to 17.1 dpa (Fig. 2f) indicates that growth of some voids has occurred between with a doubling of dose.

The observed swelling values of 0.006% – 0.033% (Table 2) in BOR60 irradiated T91 heat 30176 appear to be low compared to other T91 heats irradiated in FFTF (a commercial heat) or HFIR (an experimental heat XA3590) at similar temperatures and doses. For instance, Kai and Klueh [8] observed 0.86% of swelling in the commercial heat T91 irradiated in FFTF at 420°C to 35 dpa. The average void size is much larger (30 nm) than that in the BOR60 irradiated T91 heat 30176 (~6 nm). Interestingly, the reported average dislocation loop size (100 nm) is also much larger than the 26 nm for the BOR60 irradiation at 415°C. Both void swelling (~0.19%) and average void size (15 nm) are smaller in T91 heat XA3590 irradiated at 400°C to ~36 dpa in HFIR [5] compared to that in the FFTF irradiation. But the void swelling in T91 heat XA3590 irradiated in HFIR is still much higher than that in the BOR60 irradiated T91 heat 30176. The bimodal distribution with high density of small bubbles observed in BOR60 irradiated T91 was not reported in either FFTF- or HFIR- irradiated T91. The differences in observed swelling behavior are probably due to many factors including variations in irradiation temperature and irradiation dose, helium production rates due to spectrum differences, and/or heat-to-heat

variations as well as differences in heat treatments, all of which can affect void swelling significantly as demonstrated in FFTF irradiated HT9 [31].

Both the average void size and number density (Fig. 11b) are greater at 376°C compared to 415°C, resulting in a higher degree of swelling at 376°C. No void swelling is observed at 460°C and 524°C in BOR60 irradiated T91. As no BOR60 irradiation at temperature lower than 376°C was conducted, the peak swelling temperature cannot be determined from this series of BOR60 irradiations. It appears that the major effect of temperature is on the density of small bubbles (Fig. 2f), which is about one order of magnitude lower at 415°C than that at 376°C. The effect of small bubbles on void swelling can be very complex. On the one hand, they may serve as precursors for large voids thus promoting void swelling at high doses. On the other hand, a very high density of small bubbles increases defect sink density, which reduces void growth. The difference in small bubble density may affect void nucleation and growth at higher doses, although the effect was not seen at ~17 dpa.

Swelling is strongly affected by interstitial-biased dislocations while neutral sinks such as grain boundaries, pre-existing precipitates and radiation-induced G-phase particles lower the overall population of interstitials and vacancies by providing recombination sites. Dislocations consist of both the pre-existing dislocation network and dislocation loops formed under irradiation. The density of pre-existing dislocations, $\sim 1 \times 10^{15} \text{ m}^{-2}$, did not appear to vary significantly at the examined irradiation conditions. The dislocation loop line density of 1.4-2.0 m^{-2} (Table 2) accounted for less than 20% of the total dislocation density. Therefore, the pre-existing dislocations probably dominate the swelling behavior at the examined irradiation doses. It is well-established that the swelling rate is dependent on the dislocation/void sink strength ratio, the Q-value [32]. A low swelling rate is expected when $Q \gg 1$ which is the case for T91 in the examined dose range because of the high density of dislocations and low swelling.

4.3 Precipitate evolution

Both pre-existing Cr-carbides and V,Cr-nitrides were observed after BOR60 irradiation. Amorphization of carbides may occur at low temperatures ($< 220^\circ\text{C}$) as demonstrated by Jia and Dai [33] in T91, but in the BOR60 irradiation temperature range of 376-524°C, amorphization of carbides was unlikely. Dissolution of carbides by irradiation was reported in proton irradiated

T91 [34], which may also be the case for BOR60 irradiated T91. It is not possible to determine whether any carbides or nitrides dissolved during irradiation since the statistics based on the EDS maps was poor. Ni/Si-rich precipitates were observed in BOR60 irradiated T91 at the irradiation temperatures of 376-415°C but were not observed at 460°C and 524°C. APT revealed that these Ni/Si-rich precipitates were G-phase or its precursors. Ni/Si-rich G-phase has been reported in both ion irradiated [29,34,35] and neutron irradiated [9,24] F-M alloys. Formation of G-phase in F-M alloys is relatively understood. Cluster dynamics simulations suggest that both heterogeneous nucleation and radiation-induced segregation at dislocations are necessary for the formation of G-phase [36].

A slight increase in size and a decrease in number density (Fig. 10c) with dose indicates that precipitates are still evolving with irradiation at 376-378°C and 35 dpa. However, the volume fractions are nearly the same, ~0.04% at both doses (Fig. 10c). Getto et al. [29] reported that G-phase evolved slowly at much higher irradiation damage levels of 188-650 dpa with an increase in average size and a decrease in number density in Fe⁺⁺ irradiated HT9. The volume fraction did not change significantly at high doses. The theoretical volume fraction of G-phase in T91 assuming that all Ni (~0.1%) is consumed by G-phase is ~0.2%. As Ni and Si also segregate to dislocations, grain boundaries and other interfaces, the maximum volume fraction is expected to be much less than 0.2%. Combined with the saturation of RIS, significant increase in volume fraction of G-phase precipitates at higher doses is not expected, although the precipitate size and density may still evolve with dose.

The absence of G-phase at 460°C in BOR60 irradiated T91 was unexpected as significant segregation of Ni and Si still occurred at this temperature (Fig. 9). Anderoglu et al. [37] reported a few large G-phase precipitates observed at grain boundary triple junctions but not within the grains or laths in FFTF-irradiated HT9 at 466°C to 92 dpa. However, both Ni and Si contents in HT9 are much higher than in T91 (Ni: 0.48 vs. 0.10; Si: 0.41 vs. 0.25 in wt%). The absence of G-phase in T91 at 460°C is, therefore, not unreasonable considering the low bulk Ni and Si contents. As segregation of Ni/Si is minimal at 524°C, formation of G-phase was not expected in BOR60 irradiated T91 at that temperature.

Cu-rich clusters were observed in BOR60 irradiated T91 at 376-415°C. The solubility of Cu in α -Fe is very low (0.003 wt% at ~300°C [38]) and Cu in T91 is likely supersaturated at the BOR60 irradiation temperatures even though the bulk content is only 0.062 wt%. Radiation

enhanced formation of Cu-rich clusters was reported in proton irradiated T91 and HCM12A [34] and the volume fraction of Cu-rich precipitates was shown to be dependent on bulk Cu content. APT revealed that Cu-rich precipitates were associated with Ni/Si-rich precipitates, dislocations and grain boundaries [34]. Besides the increase in Cu solubility at higher temperatures, the lack of Ni/Si-rich precipitates and dislocation loops at 460°C and 524°C may also contribute the absence of Cu-rich precipitates at these higher temperatures.

4.4 Radiation induced segregation

Similar to dislocation loops, radiation-induced segregation at the lath boundary appeared to saturate by 17 dpa. There was negligible change in the magnitude of enrichment for Cr, Ni and Si at 35.1 dpa compared to 17.1 dpa at 376-378°C, indicating that RIS has saturated by 17 dpa (Fig. 8). Saturation of RIS occurs when the concentration gradient of the enriched element at the grain boundary rises to the level where backward diffusion balances enrichment by RIS. However, the extent of segregation increases with temperature to a maximum at 460°C. Observed enrichment of Cr, Ni and Si at the grain boundary in BOR60-irradiated T91 is consistent with proton irradiated T91 [28, 39-42] at similar irradiation temperatures. RIS behavior of Cr in F-M alloys can be explained by the diffusion coefficient ratio of Cr to Fe for both vacancies and interstitials [39, 42]. Enrichment of Cr occurs at lower temperature when the interstitial diffusion coefficient ratio dominates, and depletion occurs at high temperatures when the vacancy diffusion coefficient ratio dominates. The cross-over temperature appeared to be around 600°C for proton irradiated T91 [42]. The temperature dependence of the diffusivity ratio resulted in a maximum enrichment of Cr at ~450°C for proton-irradiated T91 [42], consistent with the observed temperature dependence of Cr enrichment in BOR60-irradiated T91 of 460°C. Minor elements Ni and Si showed a peak in segregation at a lower temperature of ~400°C, also consistent with proton irradiations [42].

It is noteworthy that while there is significant RIS at 460°C, dislocation loops, Ni/Si-rich precipitates as well as voids larger than 2 nm were all absent. Contrary to RIS that requires only the flow of defects to the sink, voids, loops and precipitates depend on a net flux of one type of defects for nucleation to occur. It appears that the net flux of interstitials or vacancies could not be maintained at a high enough level to counteract thermal emission at the irradiation temperature, so nucleation of dislocation loops and voids did not occur. The lack of nucleation of

Ni/Si-rich precipitates at 460°C may be due partially to the lack of dislocation loops as additional nucleation sites besides pre-existing dislocations.

5. Conclusions

Dislocation loops, cavities (small bubbles and voids), radiation-induced precipitates and radiation-induced segregation were examined in T91 neutron irradiated in BOR60 at 376°C-524°C to doses up to 35.1 dpa. A summary of microstructure characterization is as follows:

- Dislocation loops were observed at 376°C-415°C while only network dislocations were observed at 460°C and 524°C. The dominance of network dislocations at high temperatures of 460°C and 524°C is consistent with observations of F-M alloys in FFTF irradiations. Dislocation loops saturated at 17.1 dpa at 376°C. Dislocation loops were mainly $a\langle 100 \rangle$ type in BOR60 irradiated T91 which is also consistent with observations in FFTF irradiation.
- Voids were in the nucleation stage at 17.1 dpa and the number density as well as swelling increased with irradiation dose at 376-378°C. A bimodal cavity distribution was observed with a high density of small bubbles less than 2 nm in the temperature range 376-415°C. Only small bubbles were observed at 460°C and 524°C.
- Enrichment of Cr, Ni and Si at the grain boundary occurred at all doses and temperatures. At a temperature of 376°C RIS appeared to saturate at 17.1 dpa. Cr enrichment peaked at a temperature of 460°C, and Ni and Si enrichments peaked at lower temperatures.
- The dominant radiation-induced precipitates were the Ni/Si-rich G-phase precipitates in BOR60 irradiated T91. The average size and volume fraction increased slightly with dose and temperature but a continued increase in volume fraction was not expected at much higher doses due to the low bulk Ni content. The absence of Ni/Si-rich precipitates at 460°C was likely due to the lack of dislocation loops as additional nucleation sites. No Ni/Si-rich precipitates were observed at 524°C due to the minimal RIS of Ni and Si at the temperature. Cu-rich precipitates were observed in BOR60 irradiated T91 at 376-415°C.

Acknowledgements

The authors gratefully acknowledge Drs. M.J. Hackett, B.A. Hilton, and C. Xu at TerraPower, LLC and Dr. T. Saleh at Los Alamos National Laboratory for providing on-going support of the BOR60 irradiation campaign. The authors would also like to thank the Irradiated Materials Examination and Testing (IMET) facility and LAMDA laboratory staff for their continuing support of this research. Primary support for this research was provided by Department of Energy under contract DE-NE0000639. The atom probe tomography work was supported by the Engineering and Physical Sciences Research Council (EPSRC) funding under contract EP/L025817/1 and EP/M022803/1. Electron microscopy characterization using ORNL's LAMDA facility was supported by the Department of Energy, Office of Nuclear Energy, under DOE Idaho Operations Office Contract DE-AC07-051D14517 as part of a Nuclear Science User Facilities experiment. This research was performed, in part, using instrumentation (FEI Talos) provided by the Department of Energy, Office of Nuclear Energy, Nuclear Technology R&D (formerly Fuel Cycle R&D) Program, and the Nuclear Science User Facilities.

References

1. G.S. Was, Z. Jiao, E. Getto, K. Sun, A.M. Monterrosa, S.A. Maloy, O. Anderoglu, B.H. Sencer, M. Hackett, *Scr. Mater.* 88 (2014) 33
2. <https://neup.inl.gov/SiteAssets/FY%202013%20Abstracts/IRP/IRP-University%20of%20Michigan.pdf>
3. D. J. Edwards and S.M. Bruemmer, *Characterization of CIR II Irradiated Stainless Steels*, EPRI, Palo Alto, CA, EP-P19021/C9406, 2008.
4. F.A. Garner, M.B. Toloczko, B.H. Sencer, *J. Nucl. Mater.* 276 (2000) 123-142
5. J.M. Vitek, R.L. Klueh, *J. Nucl. Mater.* 122–123 (1984) 254–259.
6. D.S. Gelles, *J. Nucl. Mater.* 212–215 (1994) 714–719.
7. M.B. Toloczko, F.A. Garner, C.R. Eiholzer, *J. Nucl. Mater.* 212–215 (1994) 604.
8. J.J. Kai, R.L. Klueh, *J. Nucl. Mater.* 230 (2) (1996) 116.
9. J. Van den Bosch, O. Anderoglu, R. Dickerson, M. Hartl, P. Dickerson, J.A. Aguiar, P. Hosemann, M.B. Toloczko, S.A. Maloy, *J. Nucl. Mater.* 440 (2013) 91–97
10. Z. Tong, Y. Dai, *J. Nucl. Mater.*, 398 (2010) 43–48
11. L. Tan, B.K. Kim, Y. Yang, K.G. Field, S. Gray, M. Li, *J. Nucl. Mater.* 493 (2017) 12e20
12. W. Van Renterghem, D. Terentyev, M.J. Konstantinovic, *J. Nucl. Mater.* <https://doi.org/10.1016/j.jnucmat.2017.10.045>

13. C.M. Parish, N.A.P. Kiran Kumar, L.L. Snead, P.D. Edmondson, K.G. Field, C. Silva, A. Marie Williams, K. Linton, K.J. Leonard, *Microsc. Microanal.* 21 (2015) 1003–1004.
14. C.M. Parish, K.G. Field, A.G. Certain, J.P. Wharry, *J. Mater. Res.* 30 (2015). doi:10.1557/jmr.2015.32.
15. P.J. Phillips, M.C. Brandes, M.J. Mills, M. De Graef, *Ultramicroscopy.* 111 (2011) 1483–1487.
16. B. Yao, D.J. Edwards, R.J. Kurtz, *J. Nucl. Mater.* 434 (2013) 402–410
17. G. Cliff, G.W. Lorimer, *J. Microsc.* 103 (1975) 203–207
18. J. Henry, S.A. Maloy, in: Pascal Yvon (Ed.), *Structural Materials for Generation IV Nuclear Reactors*, Woodhead Publishing, 2017, Pages 329–355
19. R. Schaublin, M. Victoria, in: G.E. Lucas, L. Snead, M.A. Kirk, R.G. Elliman (Eds.), *Microstructural Processes in Irradiated Materials*, Materials Research Society Symposium Proceedings, vol. 650, 2001. R.1.8.
20. S. Dudarev, P. Derlet, R. Bullough, *J. Nucl. Mater.* 386–388 (2009) 45
21. M. Jenkins, Z. Yao, M. Hernández-Mayoral, M. Kirk, *J. Nucl. Mater.* 389 (2009) 197
22. X. Liu, Y. Miao, M. Li, M.A. Kirk, S. A. Maloy, J.F. Stubbins, *J. Nucl. Mater.* 490 (2017) 305–316
23. Y. Katoh, A. Kohyama, D.S. Gelles, *J. Nucl. Mater.* 225 (1995) 154–162
24. B.H. Sencer, J.R. Kennedy, J.I. Cole, S.A. Maloy, F.A. Garner, *J. Nucl. Mater.* 414 (2011) 237–242
25. G.S. Was and J.T. Busby, *Philosophical Magazine*, 85 (2005) 443.
26. C. Topbasi, A.T. Motta, M.A. Kirk, *J. Nucl. Mater.* 425 (2012) 48–53
27. C. Topbasi, D. Kaoumi, A.T. Motta, M.A. Kirk, *J. Nucl. Mater.* 466 (2015) 179–186
28. G. Gupta, Z. Jiao, A.N. Ham, J.T. Busby, G.S. Was, *J. Nucl. Mater.* 351 (2006) 162–173
29. E. Getto, G. Vancoevering, G.S. Was, *J. Nucl. Mater.* 484 (2017) 193–208
30. S.J. Zinkle, in: R.J.M. Konings (Ed.), *Comprehensive Nuclear Materials*, Elsevier, 2012, p. 65
31. M.J. Hackett and G. Povirk, *ANS Transactions*, 106 (2012) 1133
32. G.S. Was, *Fundamentals of Radiation Materials Science: Metals and Alloys*, Second Edition, Springer, Berlin, 2017. p. 418–425.
33. X. Jia, Y. Dai, *J. Nucl. Mater.* 318 (2003) 207–214
34. Z. Jiao, V. Shankar, G.S. Was, *J. Nucl. Mater.* 419 (2011) 52–62
35. Z. Jiao, G.S. Was, *J. Nucl. Mater.* 425 (2012) 105
36. Jia-Hong Ke, Huibin Ke, G. Robert Odette, Dane Morgan, *J. Nucl. Mater.* 498 (2018) 83–88
37. O. Anderoglu, J. Van den Bosch, P. Hosemann, E. Stergar, B.H. Sencer, D. Bhattacharyya, R. Dickerson, P. Dickerson, M. Hartl, S.A. Maloy, *J. Nucl. Mater.* 430 (2012) 194

38. G.R. Odette, G.E. Lucas, Radiat. Eff. Defects Solids 144 (1) (1998) 189–231
39. G.S. Was, J.P. Wharry, B. Frisbie, B.D. Wirth, D. Morgan, J.D. Tucker, T.R. Allen, J. Nucl. Mater. 411 (2011) 4
40. J.P. Wharry, Z. Jiao, G.S. Was, J. Nucl. Mater. 425 (2012) 117
41. J.P. Wharry, G.S. Was, J. Nucl. Mater. 442 (2013) 7-16
42. J.P. Wharry, G.S. Was, Acta Mater. 65 (2014) 42–55.

Tables and Figures

Table 1. Chemical compositions (wt%) of T91 heat 30176 provided by PNNL and Luvak.

Table 2. Summary of characterization results for Ni/Si-rich precipitates, cavities and dislocation loops in T91 irradiated at various conditions in BOR60. Error in sizes is the larger of the standard error of the mean and pixel resolution of the image. Error in number densities (not shown) is due to TEM foil thickness measurement and is estimated to be 10%.

Table 3. Summary of Cr, Ni and Si grain boundary concentrations and changes from nominal in T91 irradiated in BOR60.

Fig. 1. STEM-BF images showing dislocation evolution in T91 irradiated in BOR60 under different irradiation conditions: (a) 376°C:17.1 dpa; (b) 378°C:35.1 dpa; (c) 415°C:18.6 dpa; (d) 460°C:14.6 dpa; and (e) 524°C:15.4 dpa; (f) dislocation size distribution. Some near edge-on dislocation loops are indicated by arrows. A possible $1/2a\langle 111 \rangle$ type dislocation loop is circled in (a)).

Fig. 2. STEM HAADF images showing cavity evolution in T91 irradiated in BOR60 under different irradiation conditions: (a) 376°C:17.1 dpa; (b) 378°C:35.1 dpa; (c) 415°C:18.6 dpa; (d) 460°C:14.6 dpa; and (e) 524°C:15.4 dpa; (f) size distribution of cavities. Some cavities are indicated by arrows. The inset in (a) is under focus TEM BF images showing high density of small bubbles.

Fig. 3. EDS elemental maps showing Cr-rich carbides, V-rich nitrides, Ni/Si-rich and Cu-rich precipitates in T91 irradiated in BOR60: (a) 376°C:17.1 dpa and (b) 460°C:14.6 dpa.

Fig. 4. Ni/Si-rich clusters or G-phase evolution in T91 irradiated in BOR60 under different irradiation conditions: (a) 376°C:17.1 dpa; (b) 378°C:35.1 dpa; (c) 415°C:18.6 dpa; (d) 460°C:14.6 dpa; and (e) 524°C:15.4 dpa; (f) G-phase size distribution.

Fig. 5. Atom maps of T91 irradiated in BOR60 to 415°C:18.6 dpa.

Fig. 6. (a) (c) Ni/Si/Mn-rich clusters highlighted using iso-concentration surfaces of Mn + Ni + Si at 5 at% in two different APT tips from T91 irradiated in BOR60 to 415°C:18.6 dpa. (b) (d) Proximity histograms showing the concentrations of major elements in Cluster 1 and Cluster 2, respectively.

Fig. 7. Radiation induced segregation of Fe, Cr, Ni and Si at the grain boundary in T91 irradiated in BOR60 under different irradiation conditions: (a) 376°C:17.1 dpa; and (b) 524°C:15.4 dpa.

Fig. 8. Radiation induced segregation profiles of Fe, Cr, Ni and Si across the grain boundary in T91 irradiated in BOR60 under different irradiation conditions.

Fig. 9. Irradiation dose and temperature effect on enrichment of Cr, Ni and Si at the grain boundary in BOR60-irradiated T91.

Fig. 10. Dose effect on the average size, number density and volume fraction or line density of (a) dislocation loops, (b) void, and (c) G-phase in BOR60-irradiated T91 at 376-378°C.

Fig. 11. Temperature effect on the average size, number density and volume fraction or line density of (a) dislocation loops, (b) void, and (c) G-phase in BOR60 irradiated T91 to 17.1 dpa.

Table 1. Chemical compositions (wt%) of T91 heat 30176 provided by PNNL and Luvak.

	C	N	Al	Si	P	S	Ti	V	Cr	Mn	Ni	Cu	Nb	Mo	W	Fe
PNNL	.08	.054	-	.11	-	-	-	.21	8.6	.37	.09	-	.072	.89	-	Bal.
Luvak	.091	.052	.004	.25	.007	.002	.003	.23	8.76	.44	.10	.062	.086	.86	.004	Bal.

Table 2. Summary of characterization results for Ni/Si-rich precipitates, cavities and dislocation loops in T91 irradiated at various conditions in BOR60. Error in sizes is the larger of the standard error of the mean and pixel resolution of the image. Error in number densities (not shown) is due to TEM foil thickness measurement and is estimated to be 10%.

T (°C)	Dose (dpa)	Ni/Si-rich precipitates			Cavities				Dislocation loops		
		Average size (nm)	Number density (10^{21} m^{-3})	Vol. fraction (%)	Average void size (nm) (cavities > 2 nm)	Number density of void (10^{20} m^{-3}) (cavities > 2 nm)	Number density of bubbles (10^{20} m^{-3}) (cavities < 2 nm)	Void swelling (%)	Average diameter (nm)	Number density (10^{21} m^{-3})	Dislocation loop line density (10^{14} m^{-2})
376	17.1	5.8±0.5	3.6	0.037	6.9±1.1	7.3	1200	0.016	21.8±0.5	2.9	2.0
378	35.1	7.0±0.5	2.4	0.043	6.5±1.1	14.7	220	0.033	22.9±1.2	1.9	1.4
415	18.6	6.7±0.5	3.0	0.047	5.6±1.1	6.5	160	0.0058	25.8±0.9	2.0	1.9
460	14.6	N.O.	N.O.	N.O.	N.O.	N.O.	32	Negl.	Negl.	Negl.	Negl.
524	15.4	N.O.	N.O.	N.O.	N.O.	N.O.	33	0	N.O.	N.O.	N.O.

Table 3. Summary of Cr, Ni and Si grain boundary concentrations and changes from nominal in T91 irradiated in BOR60.

T (°C)	Dose (dpa)	Cr	ΔCr	Ni	ΔNi	Si	ΔSi
376	17.1	9.7±0.2	2.8	1.4±0.3	1.0	1.0±0.3	0.5
378	35.1	9.0±0.2	2.4	1.3±0.3	0.9	1.0±0.3	0.6
415	18.6	12.0±0.2	5.5	1.6±0.3	1.3	1.4±0.3	0.9
460	14.6	12.5±0.2	6.1	1.3±0.3	0.9	0.8±0.3	0.4
524	15.4	9.5±0.2	3.2	0.6±0.3	0.2	0.6±0.3	0.2

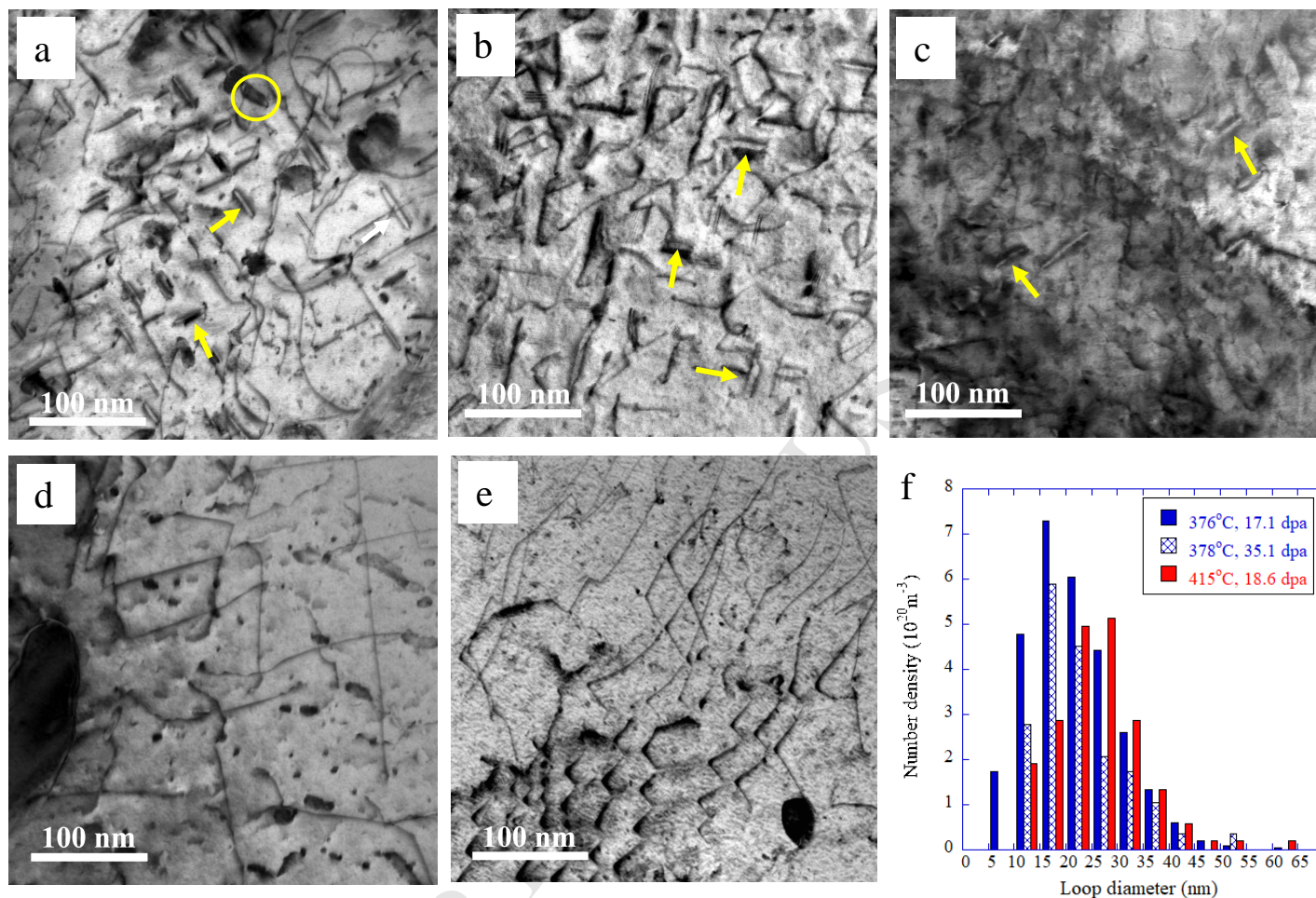


Fig. 1. STEM-BF images showing dislocation evolution in T91 irradiated in BOR60 under different irradiation conditions: (a) 376°C:17.1 dpa; (b) 378°C:35.1 dpa; (c) 415°C:18.6 dpa; (d) 460°C:14.6 dpa; and (e) 524°C:15.4 dpa; (f) dislocation size distribution. Some near edge-on dislocation loops are indicated by arrows. A possible $1/2a\langle 111 \rangle$ type dislocation loop is circled in (a).

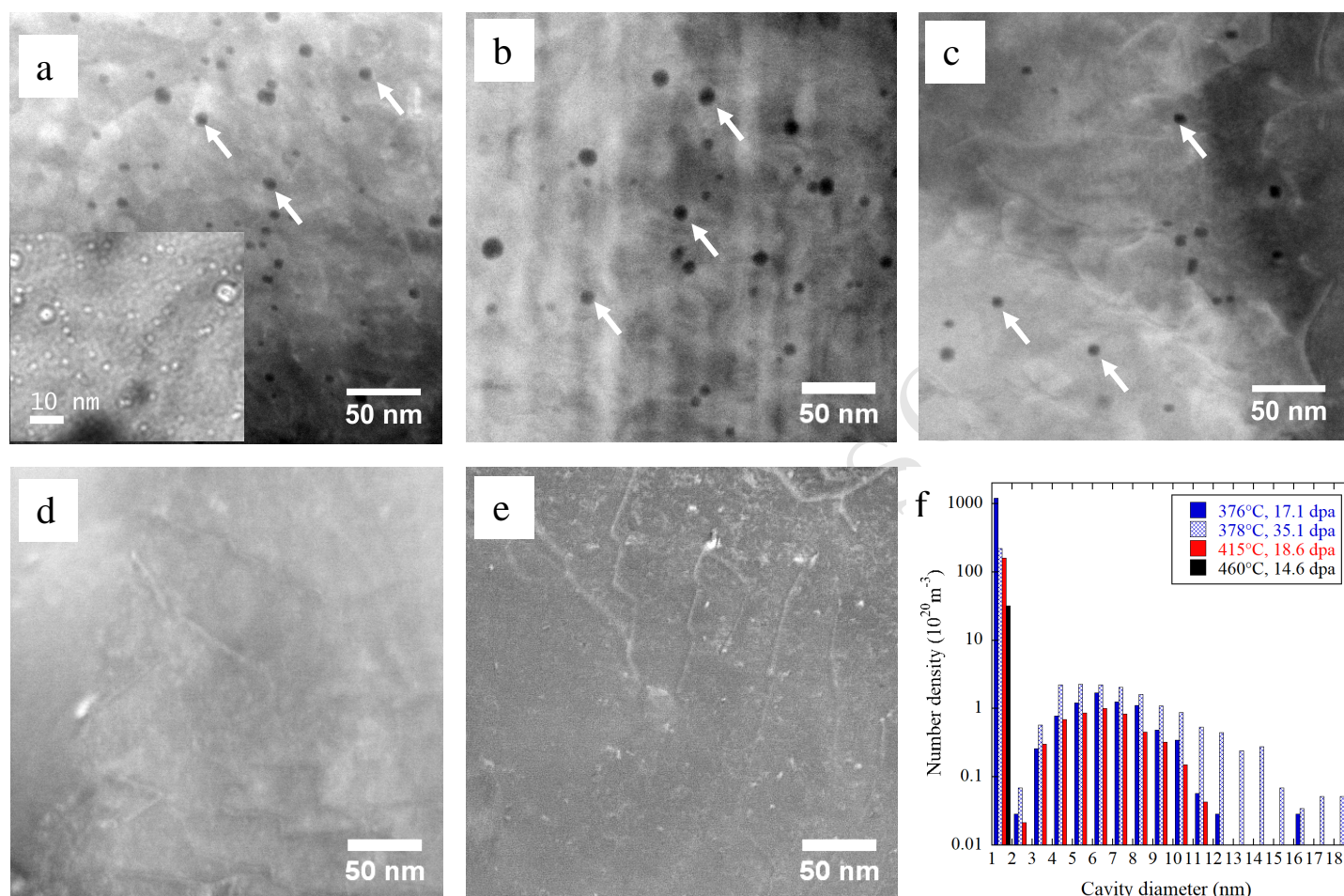
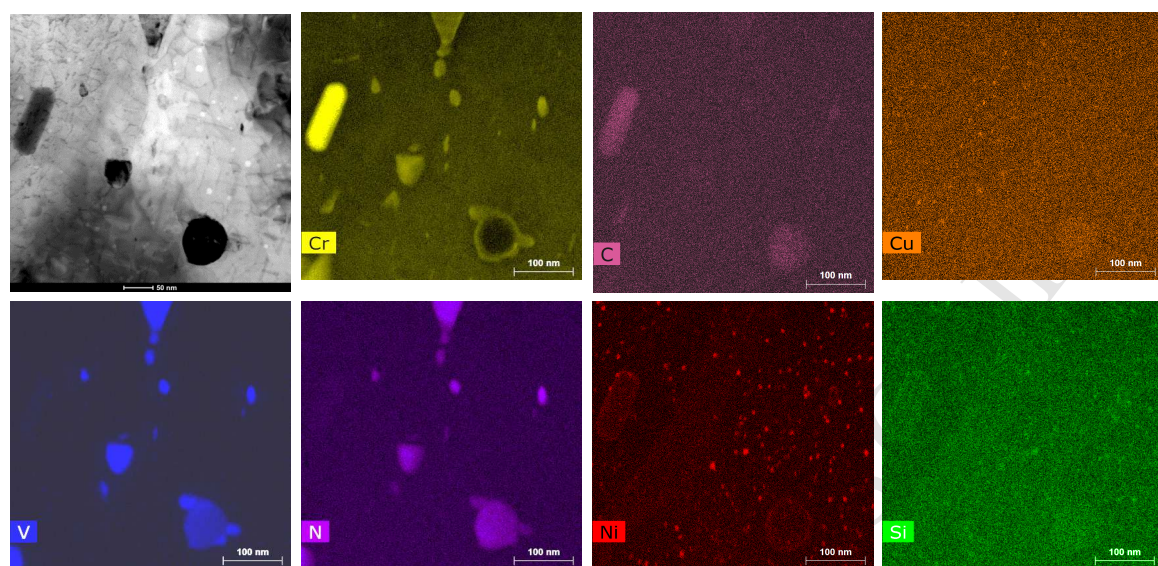
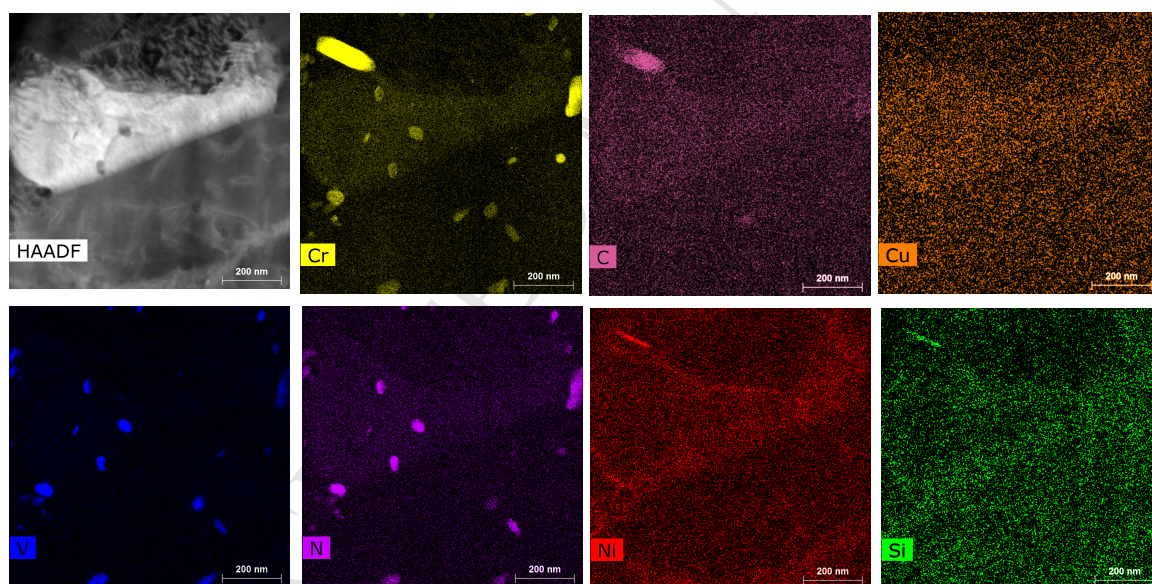


Fig. 2. STEM HAADF images showing cavity evolution in T91 irradiated in BOR60 under different irradiation conditions: (a) 376°C:17.1 dpa; (b) 378°C:35.1 dpa; (c) 415°C:18.6 dpa; (d) 460°C:14.6 dpa; and (e) 524°C:15.4 dpa; (f) size distribution of cavities. Some cavities are indicated by arrows. The inset in (a) is under focus TEM BF images showing high density of small bubbles.



a



b

Fig. 3. EDS elemental maps showing Cr-rich carbides, V-rich nitrides, Ni/Si-rich and Cu-rich precipitates in T91 irradiated in BOR60: (a) 376°C:17.1dpa and (b) 460°C:14.6 dpa.

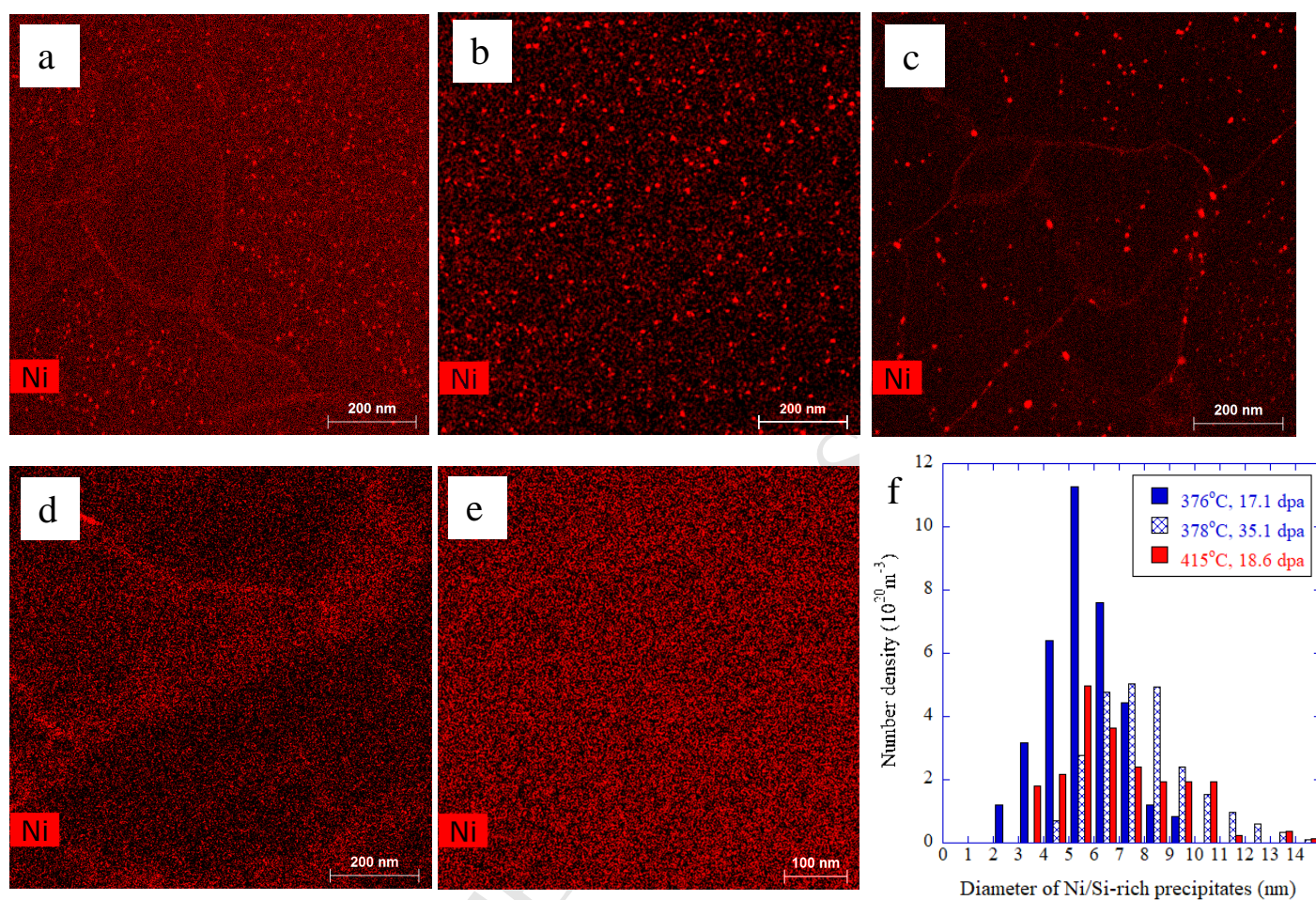


Fig. 4. Ni/Si-rich clusters or G-phase evolution in T91 irradiated in BOR60 under different irradiation conditions: (a) 376°C:17.1dpa; (b) 378°C:35.1dpa; (c) 415°C:18.6 dpa; (d) 460°C:14.6 dpa; and (e) 524°C:15.4 dpa; (f) G-phase size distribution.

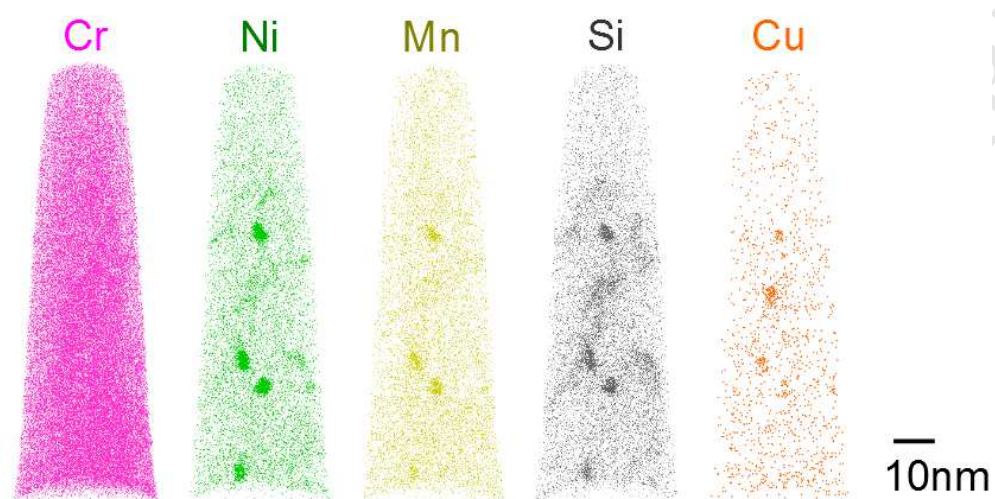


Fig. 5. Atom maps of T91 irradiated in BOR60 to 415°C:18.6 dpa.

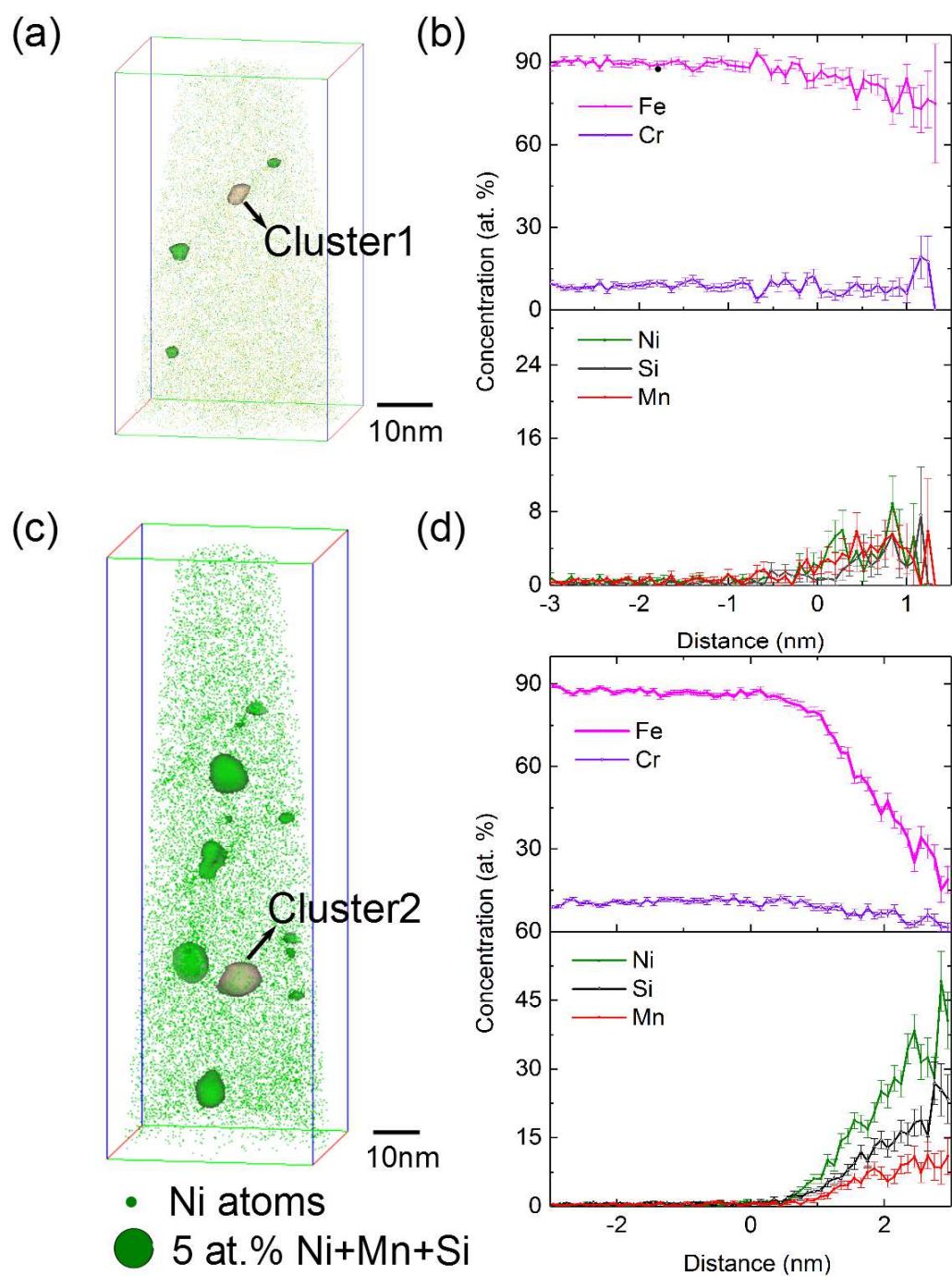


Fig. 6. (a) (c) Ni/Si/Mn-rich clusters highlighted using iso-concentration surfaces of Mn + Ni + Si at 5 at.% in two different APT tips from T91 irradiated in BOR60 to 415°C:18.6 dpa. (b) (d) Proximity histograms showing the concentrations of major elements in Cluster 1 and Cluster 2, respectively.

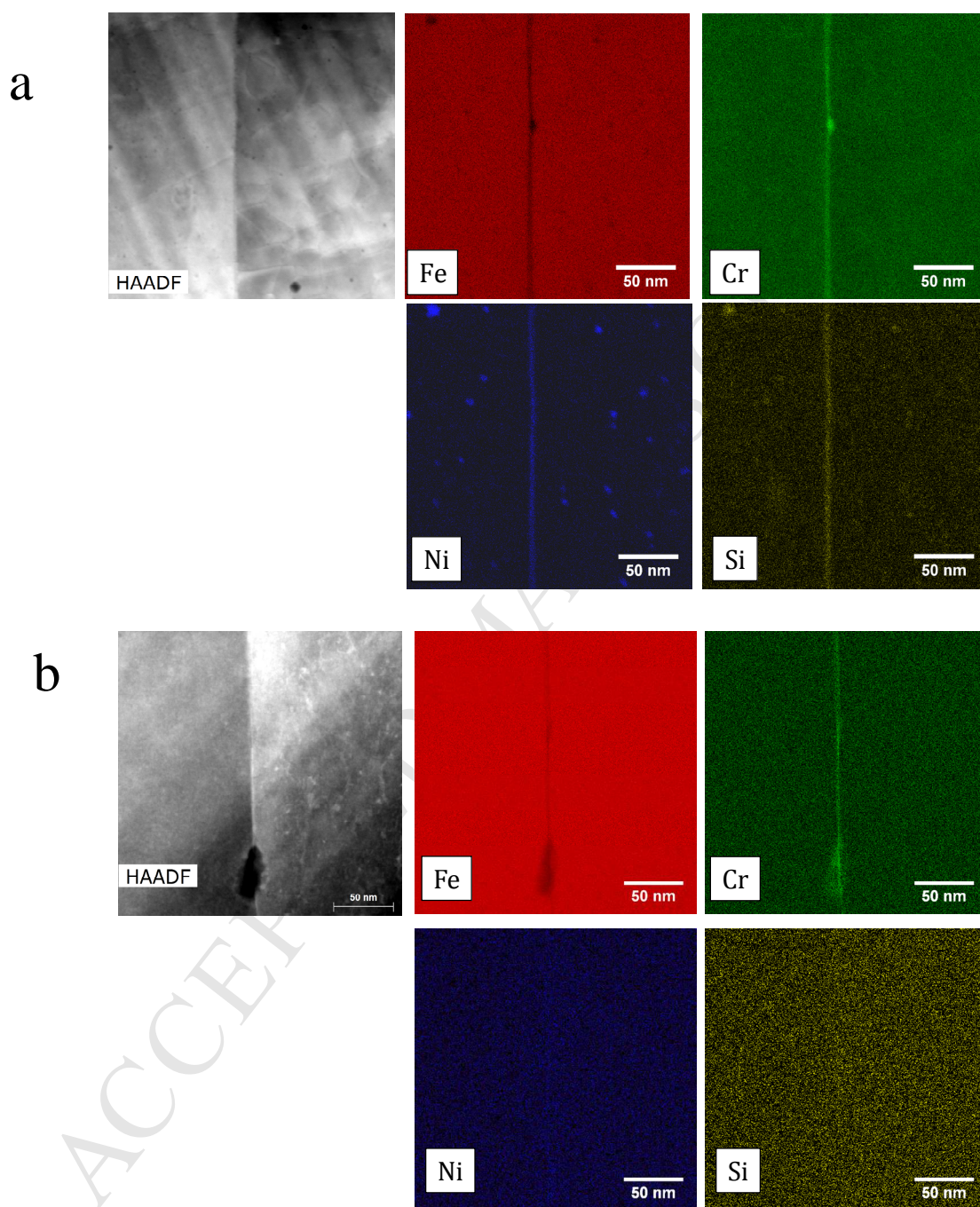


Fig. 7. Radiation induced segregation of Fe, Cr, Ni and Si at the grain boundary in T91 irradiated in BOR60 under different irradiation conditions: (a) 376°C:17.1dpa; and (b) 524°C:15.4 dpa.

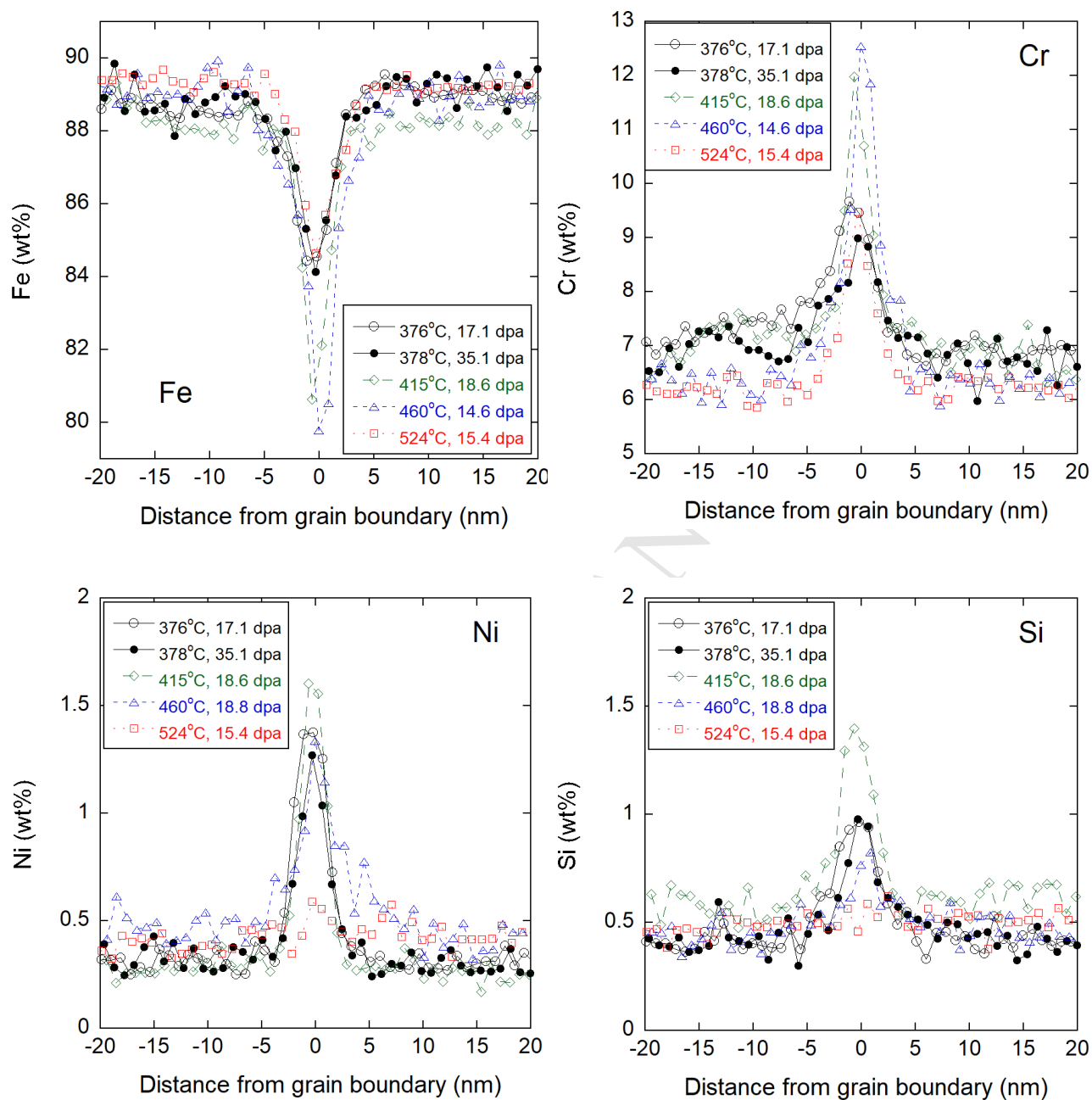


Fig. 8. Radiation induced segregation profiles of Fe, Cr, Ni and Si across the grain boundary in T91 irradiated in BOR60 under different irradiation conditions.

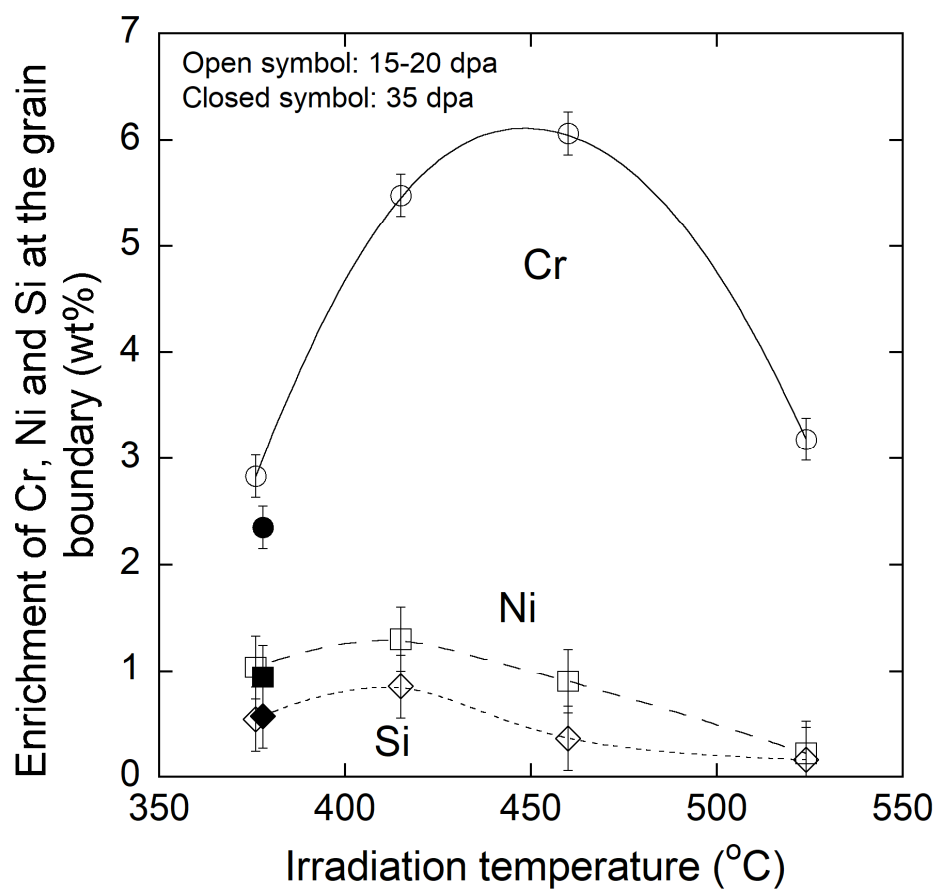


Fig. 9. Irradiation dose and temperature effect on enrichment of Cr, Ni and Si at the grain boundary in BOR60-irradiated T91.

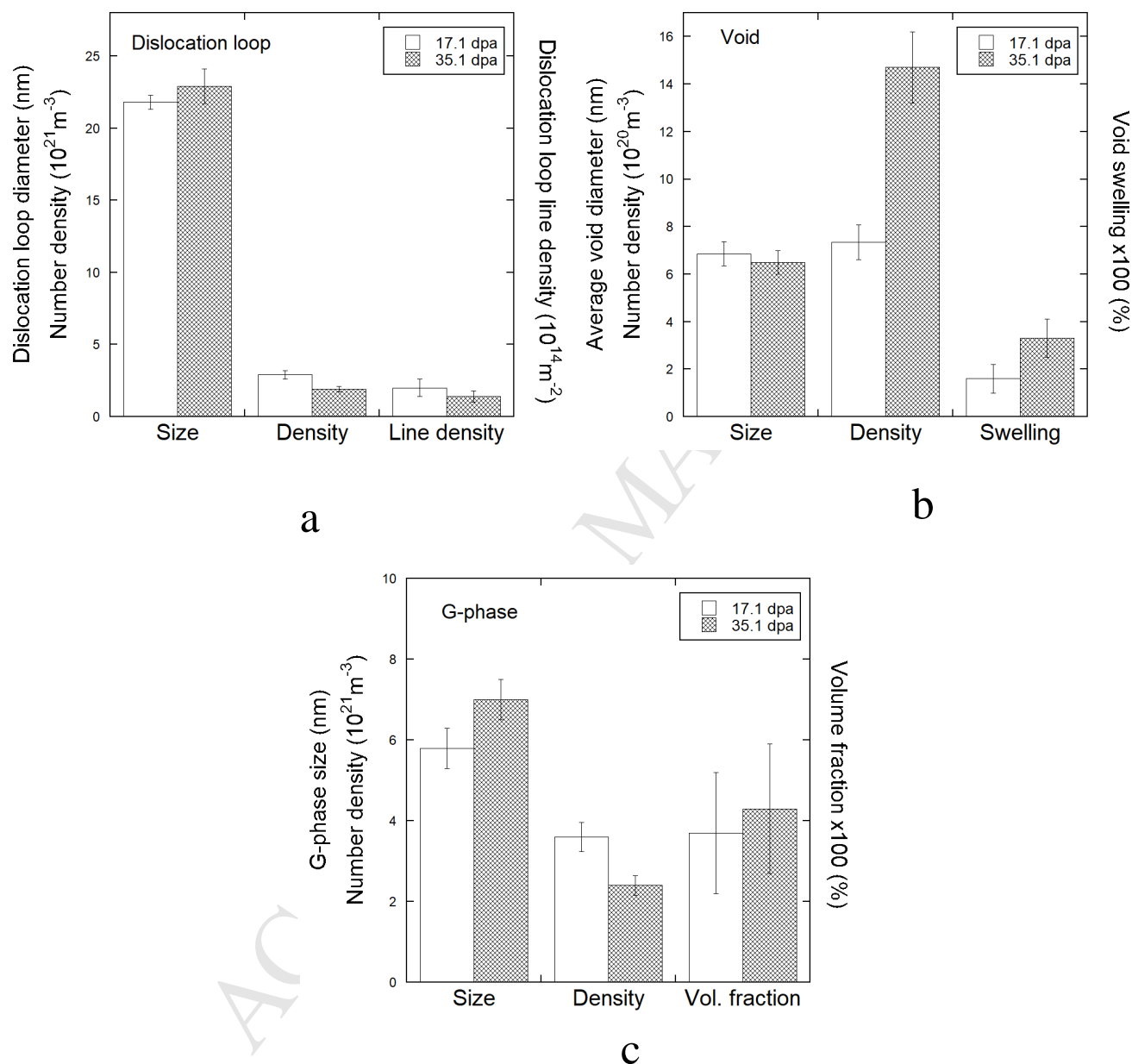


Fig. 10. Dose effect on the average size, number density and volume fraction or line density of (a) dislocation loops, (b) void, and (c) G-phase in BOR60-irradiated T91 at 376-378°C.

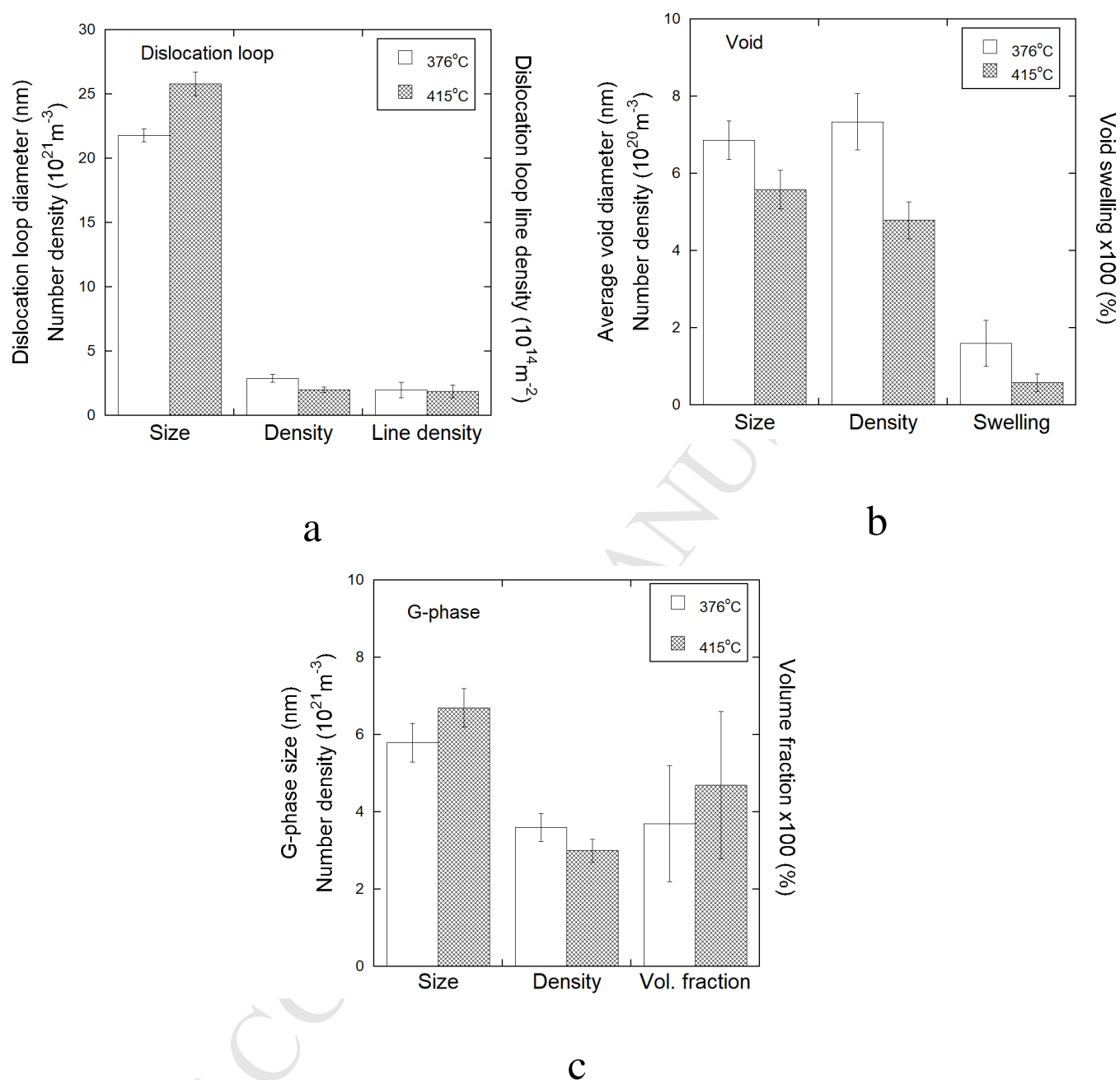


Fig. 11. Temperature effect on the average size, number density and volume fraction or line density of (a) dislocation loops, (b) void, and (c) G-phase in BOR60 irradiated T91 to 17.1 dpa.